THE JOURNAL OF PHYSICAL CHEMISTRY C

Article

Mechanistic Insight into the Photocatalytic Working of Fluorinated Anatase {001} Nanosheets

Monika Kus, Thomas Altantzis, Stephan Vercauteren, Ignacio Caretti, Ortwin Leenaerts, Kees Joost Batenburg, Myrjam Mertens, Vera Meynen, Bart Partoens, Sabine Van Doorslaer, Sara Bals, and Pegie Cool

J. Phys. Chem. C, **Just Accepted Manuscript** • DOI: 10.1021/acs.jpcc.7b05586 • Publication Date (Web): 23 Oct 2017

Mechanistic Insight into the Photocatalytic Working of Fluorinated Anatase {001} Nanosheets

Monika Kus [1], Thomas Altantzis[2], Stephan Vercauteren[3], Ignacio Caretti[4], Ortwin Leenaerts[3], Kees Joost Batenburg[5,6], Myrjam Mertens[7], Vera Meynen[1,7], Bart Partoens[3], Sabine Van Doorslaer[4], Sara Bals[2], Pegie Cool [1]*

[1] Laboratory of Adsorption and Catalysis, University of Antwerp, Universiteitsplein 1, 2610 Wilrijk, Belgium

[2] Electron Microscopy for Material Science, University of Antwerp, Groenenborgerlaan 171, 2020 Antwerp, Belgium

[3] Condensed Matter Theory, University of Antwerp, Groenenborgerlaan 171, 2020 Antwerp, Belgium

[4] Laboratory of Biophysics and Biomedical Physics, University of Antwerp, Universiteitsplein 1, 2610 Wilrijk, Belgium

[5] VisionLab, University of Antwerp, Universiteitsplein 1, 2610 Wilrijk, Belgium

[6] Centrum Wiskunde & Informatica Scientific Computing group (MAC2.1), Science Park 123, NL-1098XG Amsterdam, The Netherlands

[7] VITO - Flemish Institute for Technological Research, Boeretang 200, 2400 Mol, Belgium

* corresponding author: pegie.cool@uantwerpen.be

ABSTRACT

Anatase nanosheets with exposed {001} facets have gained increasing interest for photocatalytic applications. To fully understand the structure-to–activity relation combined experimental and computational methods have been exploited. Anatase nanosheets were prepared under hydrothermal conditions in the presence of fluorine ions. High Resolution Scanning Transmission Electron Microscopy was used to fully characterize the synthesized material, confirming the TiO_2 nanosheet morphology. Moreover, the surface structure and composition of a single nanosheet could be determined by Annular Bright-Field Scanning Transmission Electron Microscopy (ABF-STEM) and STEM Electron Energy Loss Spectroscopy (STEM-EELS). The photocatalytic activity was tested for the decomposition of organic dyes Rhodamine 6G and Methyl Orange and compared to a reference TiO_2 anatase sample. The anatase nanosheets with exposed {001} facets revealed a significantly lower photocatalytic activity compared to the reference. In order to understand the mechanism for the catalytic performance, and to investigate the role of the presence of F^-, light-induced Electron Paramagnetic Resonance (EPR) experiments were performed. The EPR results are in agreement with TEM, proving the presence of Ti^{3+} species close to the surface of the sample and allowing the analysis of the photo-induced formation of paramagnetic species. Further, *ab initio* calculations of the anisotropic effective mass of electrons and electron holes in anatase show a very high effective mass of electrons in the [001] direction, having a negative impact on the mobility of electrons towards the {001} surface and thus the photocatalysis. Finally, motivated by the experimental results that indicate the presence of fluorine atoms at the surface, we performed *ab initio* calculations to determine the position of the band edges in anatase slabs with different terminations of the {001} surface. The presence of

fluorine atoms near the surface is shown to strongly shift down the band edges, which indicates another reason why it can be expected that the prepared samples with a large amount of {001} surface, but with fluorine atoms near the surface, show only a low photocatalytic activity.

INTRODUCTION

Titanium dioxide (TiO_2) is one of the most widely used semi-conducting photocatalysts for the degradation of organic contaminants from water and air. This is due to its physical and chemical stability, high catalytic activity and low cost of production. Anatase, in comparison to the other two polymorphs rutile and brookite, is the most photocatalytically active polymorph of TiO_2. However, there are many parameters that could possibly influence the photoactivity[1] such as phase composition, electronic structure, particle size and shape[2], surface defects[3], charge transfer[4], etc. The presence of specific crystal facets plays an important role in the activity as well[5]. Surface scientists have shown that the order of average surface energies of anatase is: {001}>{100}>{101}[6–9]. The {101} facet is thus dominantly present, but unfortunately, it is not a highly reactive surface[10]. According to the Wulf construction more than 94% of crystals are dominated by {101} facets[11]. An extended review of TiO_2 with different exposed surfaces has been presented by Liu *et al.*[5]

The high reactivity of the surfaces usually diminishes during the crystal growth as a result of the minimization of surface energy. Therefore a special approach in synthesis is required. The work of Yang *et al.*[12] on the synthesis of TiO_2 anatase nanosheets with exposed {001} facets has initiated an increasing interest in the synthesis of TiO_2 materials with dominant occurrence of {001} facets [6,13–15]. It was shown by first-principle quantum-chemical calculations that the

stabilization of the {001} facet can be obtained by the adsorption of fluorine ions. Nanomaterials obtained in this manner yield 47% of {001} exposed facets. By adding hydrofluoric acid (HF) during the synthesis, an increase of this value could be achieved. The role of HF during the synthesis is dual. Primarily, it retards the hydrolysis of the Ti precursor and, secondly, it reduces the surface energy to promote the growth of {001} facets[13].

The photocatalytic activity of a {001} facet is predicted to be higher for both the decomposition of organic pollutants[13,16,17] as well as for the photocatalytic generation of hydrogen[15]. This trend is related to the higher percentage of under-coordinated Ti atoms present on this surface, which are usually more active in a heterogeneous reaction and strained configuration of the surface atoms. It is expected that the photocatalytic efficiency increases with increasing percentage of exposed {001} facets[8].

It is important to note that the reported results on the photocatalytic activity of TiO_2 with exposed {001} facets are not always in agreement[18]. Although, according to many researchers, a {001} facet is more active[13,16], it was also shown that for clean TiO_2 surfaces the order of the photocatalytic activity is {010}> {101}> {001} for the generation of hydroxyl radicals and hydrogen evolution[19]. Moreover, for the different exposed facets terminated with fluorine, the reactivity turned out to be comparable. Similar results, showing higher photocatalytic activity for {101} anatase surface, were presented by Gordon *et al.*[20]. By applying the single-molecule, single-particle fluorescence imaging technique to identify the photocatalytically active sites on individual TiO_2 nanocrystals and their composites with noble metal nanoparticles, Tachikawa *et al.*[21] proved the very important role of the {101} surface in the reduction process. Analysis of the fluorescence signal from the products of the redox-responsive fluorogenic dyes reaction revealed

that the reaction sites for the effective reduction of the dye molecules are preferentially located on the {101} surface.

The influence of fluorine ions on the photocatalytic activity of anatase nanosheets with exposed {001} facets cannot be neglected. The introduction of fluorine can be accomplished in two ways: by surface fluorination or by lattice incorporation. The surface fluorination can influence the adsorption capacity, direct hole transfer and surface electron storage[22]. Lattice fluorination induces the formation of reduced Ti^{3+} centers, and introduces special localized electronic structure and surface defect states[23]. It is known that doping of fluorine into titania might increase the photocatalytic activity[14,24]. However, it was also reported that removal of fluorine from the sample by either washing with a basic solution or by calcination improves the photocatalytic performance of anatase[25,26].

As illustrated above, the photocatalytic performance of anatase nanosheets with exposed {001} facets has been a matter of debate in literature. In this work, we present experimental results on the photocatalytic activity of TiO_2 nanosheets prepared using hydrofluoric acid. The photocatalytic activity was determined by photocatalytic decomposition of Rhodamine 6G and Methyl Orange. By using High Angle Annular Dark Field Scanning Transmission Electron Microscopy (HAADF-STEM) we were able to confirm that the TiO_2 samples are in the anatase phase and yield dominantly {001} facets. Moreover, since HAADF-STEM images are only 2-dimensional (2D) projections of a 3D object, electron tomography was used[27,28]. By applying this technique the 3D morphology of the particles, including the thickness, could be determined. Multi-frequency EPR was used to unravel the mechanism of the photocatalytic activity and to confirm the presence of Ti^{3+} sites. The experimental results were combined with theoretical *ab*

initio calculations in order to understand the behavior of the synthesized material with respect to its photocatalytic activity.

EXPERIMENTAL AND THEORETICAL METHODS

Sample preparation:

All chemicals were of analytical grade and used without further purification. All experiments were performed with the use of distilled water.

Anatase nanocrystals were synthesized by a simple hydrothermal method[13]. 0.6 mL of concentrated hydrofluoric acid (Merck) was added drop-wise to 5 mL of titanium(IV) butoxide (Acros Organics). The reaction mixture was further kept in Teflon-lined autoclave at 200°C for 24h. The sample was recovered by centrifugation and further washed three times with ethanol and distilled water. The sample was dried under vacuum at 80°C overnight and is hereafter called **ANS** (anatase nanosheet). The TiO_2-reference anatase sample was purchased from Sigma Aldrich. Fluorine doped TiO_2 reference sample was prepared by mixing 2g of powder obtained from Sigma Aldrich with 0.5 ml HF and 50 ml water for 1h. The sample was further centrifuged and dried at 80°C overnight.

Experimental characterization methods:

Transmission Electron Microscopy (TEM): HAADF-STEM, ABF-STEM and STEM-EELS measurements were performed using a monochromated aberration corrected 'cubed' FEI-Titan electron microscope operated at 120 and 200 kV. A probe convergence semi-angle of 21 mrad was used. STEM Energy Dispersive X-ray spectroscopy (STEM-EDS) measurements were performed using a FEI Osiris electron microscope operated at 200 kV, equipped with a

ChemiSTEM[29] system. For the acquisition and quantification of the EDS elemental maps, the ESPRIT software was used. Electron tomography series was acquired in HAADF-STEM mode using a FEI Tecnai G2 electron microscope operated at 200 kV. A Fischione tilt-rotation tomography holder (model 2040) was used and tomography series were acquired automatically using the Xplore 3D software. The series were acquired within a tilt range from -70˚ to +70˚ and a tilt increment of 2˚. The alignment of the series was performed using the Inspect 3D software and the reconstruction using the Discrete Algebraic Reconstruction Technique (DART)[30].

X-ray diffraction (XRD): XRD patterns were collected on a Panalytical X'Pert PRO MPD diffractometer using CuKa radiation in 2h mode with a bracket sample holder. Measurements were done at a scanning speed of 0.04°/4s continuous mode.

UV-visible Diffuse reflectance (UV-DR) spectroscopy: UV DR measurements were performed on a Thermo-electron Evolution 500 UV-Vis spectrometer equipped with RSA-CU40 Diffuse Reflectance cell. The instrument measured intensity I (of the sample diluted in KBr) and intensity I_0 (of pure KBr background), converting that directly in the software into an absorbance value according to $A=\log (I_0/I)$. From UV-Vis DR spectra information on the band-gap energy was obtained.

Electron paramagnetic resonance (EPR): X-band (~9.44 GHz) continuous-wave (CW) EPR was measured at 10 K on a Bruker ESP300E spectrometer equipped with a gas-flow cryogenic system (Oxford, Inc.). All X-band EPR spectra were recorded using a microwave power of 0.5 mW, a modulation amplitude of 0.2 mT and a modulation frequency of 100 kHz.

W-band (~94 GHz) EPR experiments were carried out on a Bruker Elexsys E680 spectrometer equipped with a continuous gas-flow cryostat (Oxford Instruments). The CW-EPR spectra were recorded at 50K, using a microwave power of 2.2 μW, a modulation amplitude of 0.4 mT and a

modulation frequency of 100 kHz. The field-swept Electron-Spin-Echo (ESE) detected EPR was acquired at 10K with the pulse sequence $\pi/2–\tau–\pi–\tau–echo$, where $t_{\pi/2}$ = 120 ns, t_{π} = 240 ns and τ=700 ns, and a repetition rate of 100Hz. This low repetition rate was needed to allow the spin system to recover equilibrium between pulse sequences due to the slow electronic relaxations of the radical species detected.

The light-induced EPR spectra were obtained with an illumination wavelength of 350.7 nm from a Kr-ion laser (Spectra Physics 2580), and a laser power of 10 mW. At X-band, a deuterium lamp with a 220 nm broadband interference filter was also used as excitation source, at a lamp current of 1.5 A. Comparisons were made between light-induced X-band CW-EPR experiments performed while pumping the sample tube (1 mbar) and experiments with the sample tube open to air. Besides a slight intensity increase of the EPR features of the contributions I-II (Table 2), O_2 induced no essential changes in the EPR spectra. The X-band EPR spectra depicted in this manuscript are recorded under air. At W-band, the sample was introduced in the EPR spectrometer at room temperature and the cavity (and sample tube) was vacuum pumped prior to cooling. All EPR spectra were recorded during light irradiation at different times of illumination. Longer illumination only led to a gradual increase of the overall EPR intensity, not to spectral changes.

All EPR spectra were simulated using the EasySpin program, a MATLAB toolbox developed for EPR simulations[31].

Nitrogen sorption: The surface area and porosity of the prepared materials were determined via N_2-sorption on a Quantachrome Quadrasorb SI automated gas adsorption system. Before measurements samples were degassed at 150°C for 16 hours. After degassing, N_2-sorption was

carried out at -196°C. The Brunauer–Emmet–Teller (BET) method was applied to calculate the specific surface area.

Energy dispersive X-ray spectroscopy (EDX): Elemental analysis was performed on a FEI QUANTA FEG 250 microscope equipped with a field emission gun. Powder was applied on the carbon tape and measured. The software used for analysis was INCA (Oxford Instruments).

Photocatalytic tests: The photocatalytic activity was tested by photodegradation of the dye molecules Rhodamine 6G (cationic dye) and Methyl Orange (anionic dye). For the experiment 8 mg of catalyst was dispersed in 50 mL of $4 \cdot 10^{-5}$ M dye solution and stirred for 40 min without UV-irradiation to obtain an adsorption-desorption equilibrium. Then the solution was irradiated for 3h under UV light (365 nm) from a 100 Watt Hg-lamp (Sylvania). During this period, 5 mL aliquots were taken out of the suspension at fixed intervals of 30 min and analyzed both by UV-Vis spectroscopy and total organic carbon (TOC) analysis. The decolorization efficiency was followed via the absorbance measured at 526 nm for Rhodamine 6G and 507 nm for Methyl Orange, with water as reference. From each sample taken for the UV-Vis analysis 0.6 mL was used for μV-TOC-analysis[32] (the remaining sample, after UV-Vis measurement, was put back to the photocatalytic reaction vessel). Using this 0.6 mL volume, two separate measurements were performed in which i) the total amount of carbon (TC) was measured and ii) the total amount of inorganic carbon (IC) was determined. For both TC and IC measurements 3 sequential injections were performed (50 μL was injected for TC and 150 μL was injected for IC). Samples for TC analysis were injected directly on the combustion oven, using the special designed gas injection kit. Samples for IC analysis were injected directly on the acid containing vile. The TOC-value was calculated as the difference between TC and IC values. The detection limit for the TOC

measurement is 50 µg/L. Photocatalytic tests were performed at room temperature and ambient atmosphere.

Computational methods:

Ab initio calculations were performed within the Density Functional Theory (DFT)[33,34] formalism as implemented in the VASP code, using the Projector Augmented Wave method[35]. The Ti ($3s^2$ $3p^6$ $4s^2$ $3d^2$), O ($2s^2$ $2p^4$), H ($1s^1$) and F ($2s^2$ $2p^5$) electrons were treated as valence electrons. The Exchange-Correlation potential was treated in the Local Density Approximation + U (LDA+U) approach [36,37] To describe the strong correlation of the Ti 3d electrons, a value of U=3 eV was applied. The choice for the LDA+U method instead of the GGA+U method was motivated based on the results presented in Arroyo-de Dompablo *et al.*[38], which showed that much better structural parameters are obtained for TiO_2 within LDA+U. A plane-wave basis set with a cutoff energy of 600 eV was used. Potentials with 12 valence electrons for Ti-atoms and 6 valence electrons for O-atoms were used.

The band structure of electrons and holes in anatase were calculated using the 12-atom tetragonal unit cell of anatase using a 9x9x3 Monkhorst-Pack k-point grid to sample the Brillouin zone, resulting in 30 k-points in the irreducible part of the Brillouin zone. Effective masses were calculated with the finite difference method using the EMC (Effective Mass Calculator) code[39].

In order to obtain the band edge shifts for different surface terminations, supercell calculations with 48 atoms were performed. For these, a 9x9x1 Monkhorst-Pack grid was used, resulting in 25 points in the irreducible Brillouin zone. The band edge shifts were obtained by directly comparing the band edge positions in the center of the slab with the potential in vacuum.

All systems were allowed to relax using a conjugate-gradient algorithm until all forces fell below 0.01 eV/Å.

RESULTS AND DISCUSSION

The overall anatase crystal structure of the TiO_2 nanosheets was first confirmed by XRD measurements (Figure S1, supporting information). In Figure 1a, a HAADF-STEM overview image of the anatase nanosheets (ANS) is presented.

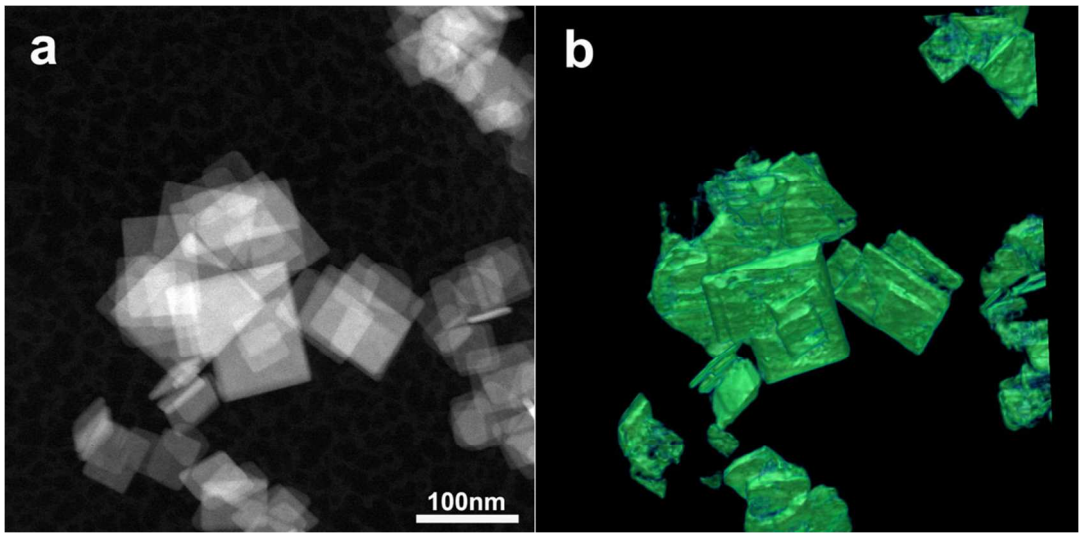

Figure 1. a) HAADF-STEM overview image of anatase nanosheets. b) 3D representation of the reconstructed volume.

Figure 1b presents a 3D representation of the reconstructed volume of the anatase nanosheets (ANS), shown in Figure 1a. Due to the fact that the particles are very thin and highly agglomerated, "missing wedge" artefacts may hamper the quantification procedure and also the facets may not be well presented[25]. In order to improve the results, a more advanced reconstruction algorithm, the so-called DART, was used in Figure 1b [40,41]. From the

reconstruction the thickness of the nanosheets could be determined to be varying between 4 and 10 nm.

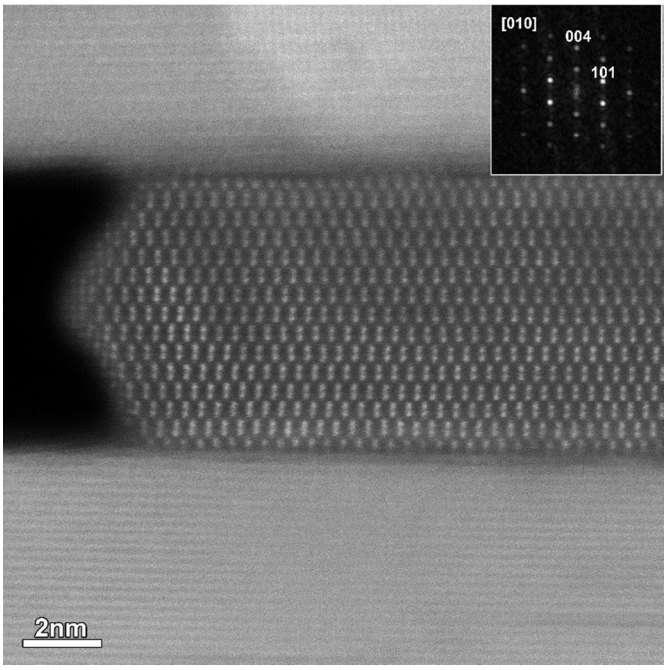

Figure 2. High resolution HAADF-STEM image of an anatase nanosheet, oriented along the [010] zone axis.

Figure 2 shows a high-resolution HAADF-STEM image of an anatase nanosheet, oriented along the [010] zone axis, as proven by the fast Fourier transform (FFT) pattern displayed in the inset. By combining this result with the morphological information obtained by electron tomography, we could verify that the top and bottom facets of the nanosheets correspond to {001} planes. HAADF-STEM images yield a contrast that scales with the atomic number Z of the elements present in a sample. Although the Ti columns can be observed, the intensity of the O columns is very low. To visualize the position of the O columns in the structure and to determine the terminating atomic layer of the nanosheet, ABF-STEM measurements were performed. This

technique is ideally suited to visualize light elements and was previously used to visualize H atoms in a YH_2 crystal[42].

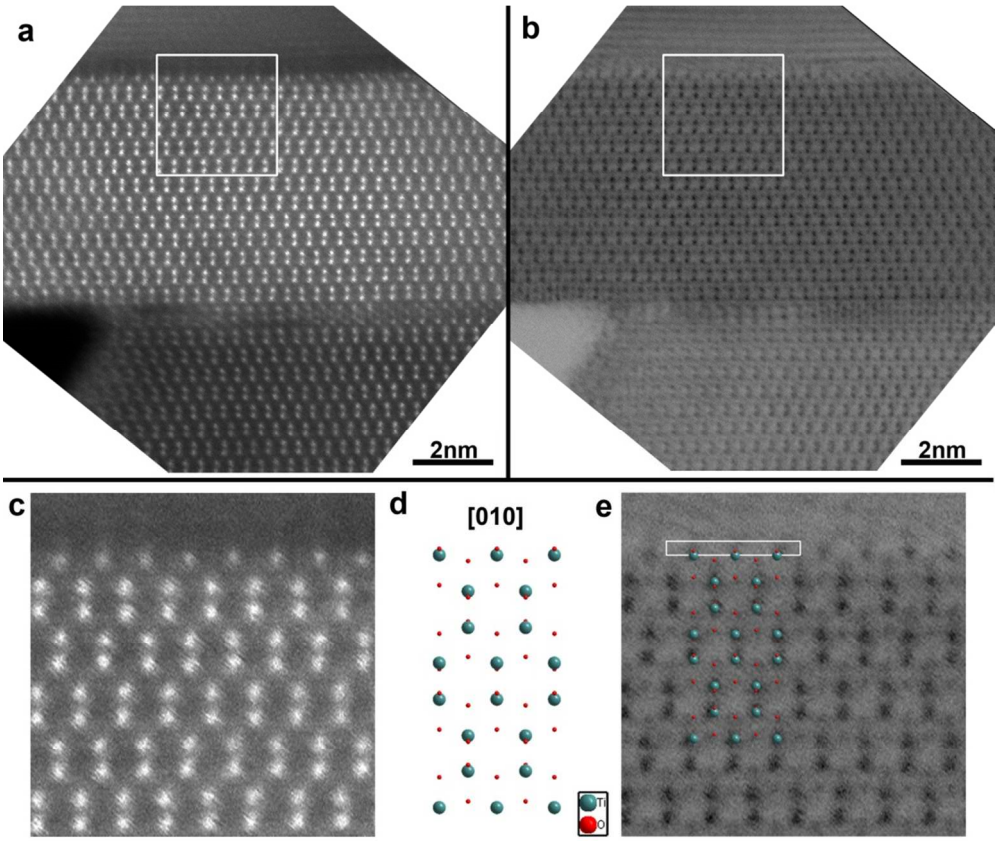

Figure 3. a) High Resolution HAADF-STEM image of an anatase nanosheet, oriented along the [010] zone axis and b) the corresponding ABF-STEM image. c) Magnified image of the region indicated by the white square in (a), d) XRD model oriented along the same zone axis with the nanosheet in (a) and (b) and e) magnified image of the region indicated by the white square in (b).

Figure 3b shows an ABF-STEM image of a nanosheet oriented along the [010] axis, in which both the Ti and O columns can be observed. In

Figure 3d, a model of the structure as obtained from X-ray diffraction (XRD) analysis is presented along the same crystallographic orientation [43]. In

Figure 3e, a more detailed part of Figure 3b (white square) is shown along with the model structure. In this manner, we conclude that the terminating plane is formed by columns of light atoms, indicated by the white rectangle in Figure 3e.

In order to determine the elemental composition of these columns, STEM-EDS measurements were performed on three nanosheets, connected along their {001} facets (Figure 4). From the STEM-EDS maps it is clear that F is present together with O on the interface between the nanosheets. The excess of F at the interface between the nanosheets can be attributed to the higher sensitivity of the exposed facets towards the electron beam.

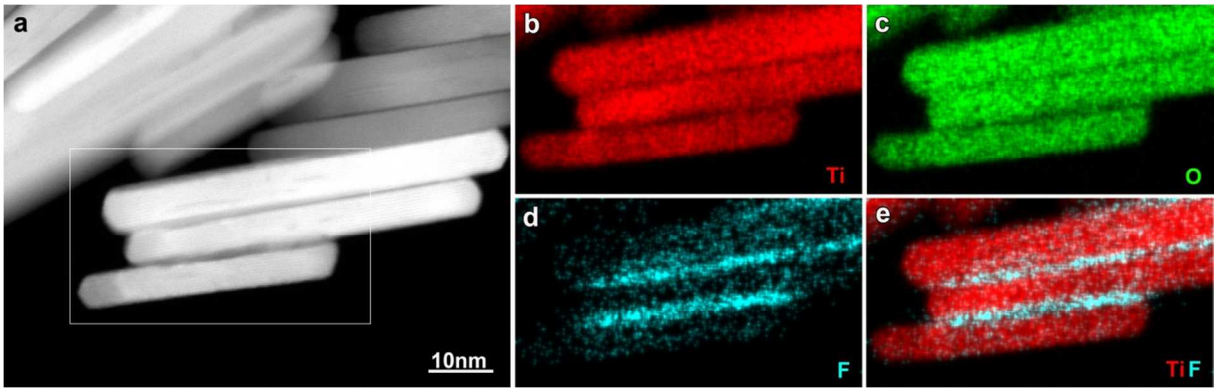

Figure 4. a) HAADF-STEM image of three anatase nanosheets, connected along their {001} facets and b-e) STEM-EDS maps acquired from the region indicated by the white rectangle in a. It can be clearly observed that an excess of F is present at the interface between the nanosheets.

An EDS spectrum of the sample is given in Figure S2 (Supporting information).

Furthermore, monochromated STEM-EELS measurements performed on a single nanosheet (Figure 5) show that the middle of the sheet corresponds predominantly to anatase (Ti^{4+}) whereas the atomic layers near the surface contain predominantly Ti^{3+}.

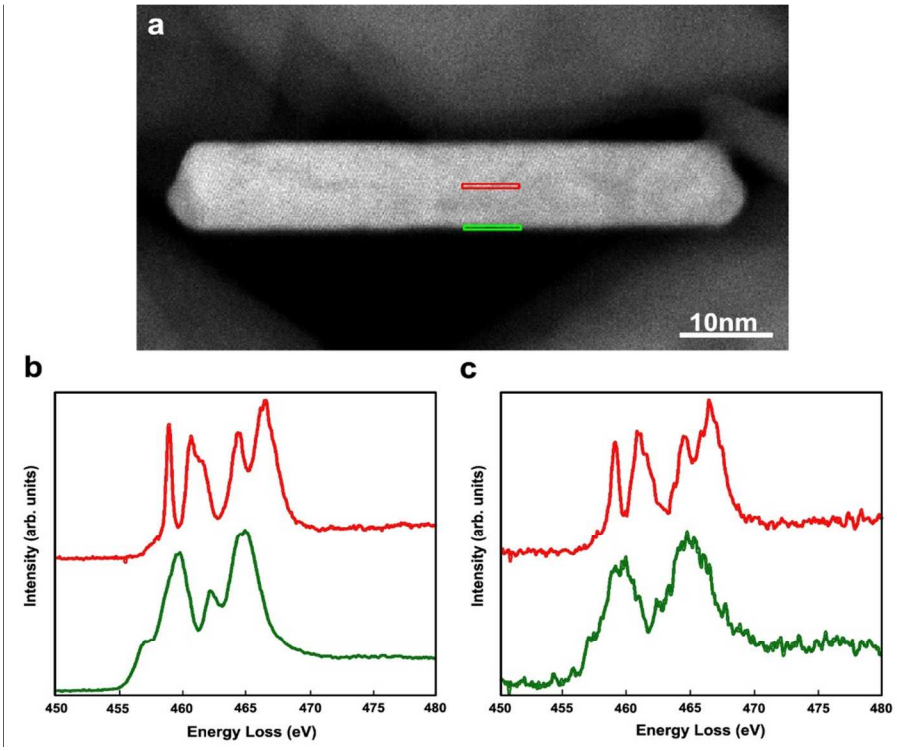

Figure 5. a) HAADF-STEM image of an anatase nanosheet, b) reference EELS spectra for Ti^{4+} (red) and Ti^{3+} (green), respectively, acquired by reference samples (pure anatase Ti^{4+} and pure Ti^{3+} samples) by using the same experimental conditions and c) EELS spectra from the surface (green) and bulk (red) parts of the region indicated by the green and red rectangles, respectively. The spectrum of the middle of the nanosheet corresponds to anatase (Ti^{4+}) whereas that of the layers near the surface corresponds more to a Ti^{3+}- rich environment.

In order to compare the photocatalytic activity of ANS to the reference anatase sample (TiO_2-reference), its ability to decompose an organic dye was tested. The UV-DR spectra and calculated

band gap energies of both samples are given in Figure S3, supporting information[44]. Table 1 represents the results of the degradation of a Rhodamine 6G solution. All samples show only a limited adsorption of the pollutant during the first 40 min in dark. However, the difference between the activity of ANS and the commercial anatase reference sample (TiO_2-reference) under UV illumination is obvious (Figure 6). The decolorization process with the commercial sample occurs much faster than with the ANS nanosheets. Although more than 99% of the dye is photobleached already after 180 min of UV irradiation for the reference sample, this is only around 43% for ANS (Figure 6). The photomineralization process was also determined by μ-volume TOC for both samples. The total degradation towards CO_2 and H_2O is again better for the TiO_2 reference sample than for synthesized ANS material. Nevertheless, although UV illumination using the commercial anatase induced almost complete photobleaching, only 25% of the Rhodamine 6G was effectively photomineralized. The ANS performed even worse: only 6.4% of the original Rhodamine 6G could be photomineralized .

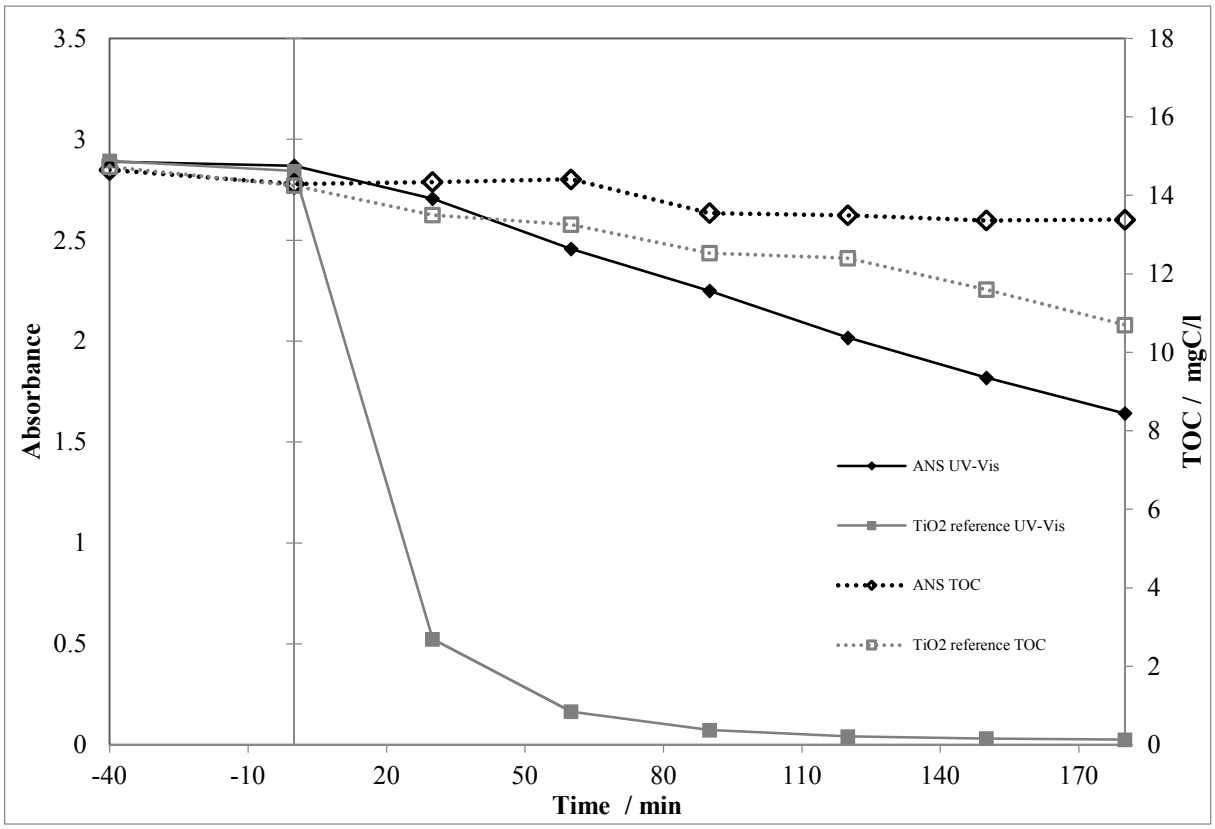

Figure 6. Photocatalytic decomposition of Rhodamine 6G by synthesized (ANS) and commercial (TiO_2 reference) photocatalysts at RT and ambient air. After obtaining the adsorption- desorption equilibrium (40 min) samples were irradiated for 180 min under UV light (365 nm) using a 100 Watt Hg-lamp (Sylvania).

Table 1. Surface area, elemental analysis and summary of photocatalytic activity of Rhodamine 6G (cationic) for both catalysts after 40 minutes of adsorption without irradiation and 180 minutes of irradiation. The obtained total percentage of degradation was calculated after 180 min of irradiation. Percentages are calculated based on the difference in absorbance values (by UV-VIS analysis), and the difference in the amounts of carbon in mg C/l (by TOC analysis).

Sample name	ANS		TiO_2 -reference	
Surface area (m^2/g)	62		12	
Fluorine content (w%)	2.46		0.00	
Analysis	*UV-Vis (%)*	*TOC (%)*	*UV-Vis (%)*	*TOC (%)*
adsorption	0.7	2.5	1.7	3.3
catalysis	42.8	6.4	99.1	24.9
total	43.2	8.7	99.1	27.4

Liu et al.[45] performed photocatalytic degradation tests towards Methyl Orange and Methylene Blue on three different surfaces of hollow TiO_2 microspheres. Fluorinated surfaces (Ti-F terminated {001} facet) showed an opposite photocatalytic selectivity towards differently charged azo dyes in comparison to clean {001} facets and Ti-OH terminated {001} facets. In the work of Liu *et al*., the fluorinated surface sample showed a preferential decomposition towards the cationic dye Methylene Blue, but it is worth mentioning that the sample contained only around 20% of exposed {001} facets. In the work of Zhu et al.[46] it was shown that the selectivity of photocatalytic conversion can be changed by changing the absolute surface area of the {001} facets. Since the photocatalytic activity towards azo dyes is greatly affected by the surface chemistry of the catalyst[45,47], a similar photocatalytic experiment was performed in our work for the degradation of the anionic dye Methyl Orange (Figure S4a, supporting information). The photocatalytic decomposition of Methyl Orange by ANS was not better than the corresponding decomposition of Rhodamine 6G, showing that in case of the synthesized ANS sample the low measured photocatalytic activity is not caused by the nature and charge of the pollutant. Furthermore, in order to check the effect of fluorine on the catalytic performance, the

photocatalytic degradation of Rhodamine 6G on a TiO_2 reference sample doped with fluorine ions has been performed. The results do not show much difference in comparison to the reference TiO_2 sample without fluorine (Figure S4b, supporting information).

To understand the mechanism of the photocatalytic activity and to corroborate the data obtained by electron microscopy, light-induced EPR experiments were performed. Figure shows the normalized experimental (a, b) and simulated (a', b') X-band CW-EPR spectra of the anatase TiO_2 nanosheets (ANS) recorded at 10K before and after excitation at 10K with a 350.7 nm laser light for 1h and 30 min under air conditions. Figure S5 shows the relative intensity of the spectra (supporting information). Comparative measurements with continuous pumping of the sample tubes (to 1 mbar) led to a small reduction of the overall intensity of contributions I-II, but no essential changes in the composition of the spectrum (see details in the experimental section). Similar spectra were obtained when using a deuterium lamp with a 220 nm broadband UV filter (see Figure S6, supporting information).

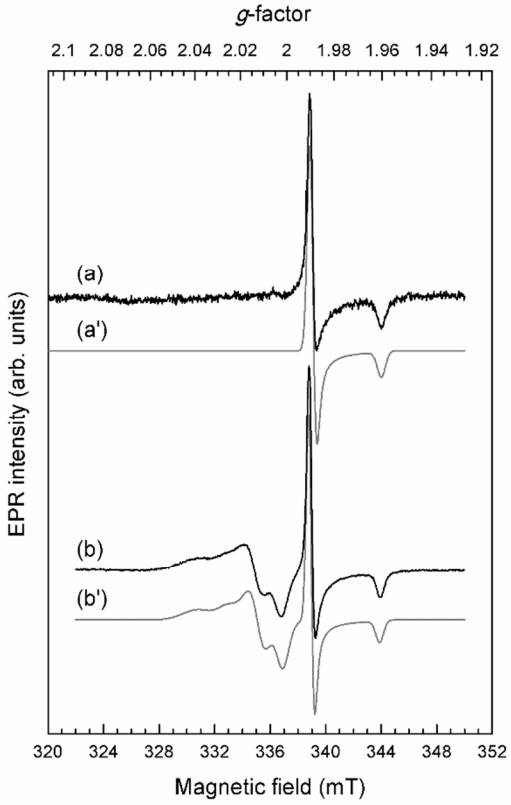

Figure 7. X-band CW-EPR spectra of ANS recorded at 10K before (a) and after (b) illumination in air with 350.7 nm laser light for 1h30min. The corresponding simulations (a') and (b') are depicted in grey under the experimental spectrum (see Figure S6 for detail, supporting information). The spectra are shown normalized for comparison.

Before illumination, spectrum 7(a) consists of a narrow axial feature with a line width of ~0.5 mT characteristic of Ti^{3+} species in anatase titania[23,48–50]. The $g<g_e=2.0023$ values of this axial $\boldsymbol{g}$ tensor are $g_{x,y}=1.99004$ and $g_z=1.95925$ (Table 2) and can be unambiguously assigned to bulk Ti^{3+} lattice ions[23,48–50]. The origin of native bulk Ti^{3+} species is well established for anatase TiO_2 materials in the presence of an electron donor. This is the case of TiO_2 prepared by wet chemistry

involving the use of HF, like in the current study, where the inclusion of F^- as dopant in O^{2-} lattice sites produces electron localization on Ti^{4+} ions and their reduction to Ti^{3+} for charge compensation[23,50,51]. The Ti^{3+} is situated on a bulk regular position of the anatase lattice not associated with oxygen vacancies[51]. Notice that surface Ti^{3+} centers have in general significantly lower g values of $g_{x,y}$~1.95-1.92 and g_z~1.9 -1.8 or may produce a broad signal around g~1.93 due to strain effects[48,49,51–53]. The latter species have not been detected here by neither X-band CW EPR nor W-band CW and ESE-detected EPR (see below). Besides, exposure of surface Ti^{3+} species to air before illumination should lead to the formation of stable oxygen-based radicals via the reaction[54]

$$Ti^{3+}_{surface} + O_2 \rightarrow Ti^{4+} + O_2^-(surface),$$

as reported for different reduced surfaces of TiO_2, but they are not observed in the present case (Figure 7a).

After 1h and 30 min UV illumination under air at 10K we observe both an increase of the Ti^{3+} EPR signal (Figure S5) and the appearance of new EPR signals at $g>g_e$ associated with a minimum of three overlapping species, labeled I-III (Figure 7b). The principal g values of these paramagnetic species are summarized in Table 2, and the separate contribution to the simulated spectrum (b') is presented in Figure S7. Two oxygen radical centers (I-II) have been identified by simulation, which are the products of (surface) photoreactions involving the generated electron and hole charge carriers. Signal I has g values typical of surface O^- species formed by hole trapping at surface O^{2-} sites: Ti^{4+}-O^{2-}+h^+→ Ti^{4+}-O^-[51,55,56]. The degree of ***g***-tensor rhombicity points to a surface rather than sub-surface defect[57]. The photoactivity of titanium dioxide materials has been shown to depend also on the surface-adsorbed water[58] and water is found to

stabilize the surface hole[57]. The presence of surface water may explain the observation of center I in these samples.

Signal II is characterized by a quite anisotropic ***g*** tensor and broad linewidths (Figure S7). Centers with similar *g* values have been assigned to $HO_2^{\bullet}$ species on titania surface sites[59–61]. These surface $HO_2^{\bullet}$ radicals may be generated through the reaction $e_{CB} + H^+ + O_2$ (surface) → $HO_2^{\bullet}$ (surface), but alternative formation processes can be considered. $HO_2^{\bullet}$ can occur through transient formation of O_2^- and subsequent protonation. It can also result from light-induced formation of $^{\bullet}OH$ radicals with subsequent reaction to H_2O_2, which in turn can react with the titanium dioxide surface to yield $HO_2^{\bullet}$ (or O_2^-)[62]. Both of the latter processes would be facilitated by the presence of accessible surface titanium atoms, which seems contradicted by the previous data. The protons needed in all three formation processes can result from surface hydroxy groups, which are not unexpected for TiO_2 prepared by wet methods. Surface hydration may also result as charge compensation for fluoride incorporation in the structure[63]. Moreover, these oxygen-centered radicals in ANS completely disappear after annealing to room temperature and recooling to 10K to measure the CW-EPR spectrum (see Figure S6c, supporting information). The thermal instability of these species has been consistently reported for partially hydrated P25[59]. Although the *g* values of center II have been assigned to $HO_2^{\bullet}$ by several authors[59–61], EPR studies of these radicals on different (non-titania) inorganic materials have shown that a large proton hyperfine coupling of 1.1-2 mT should be visible[64]. This coupling was not observed, but could be masked by the broad linewidth. Because of this, the assignment of center II to $HO_2^{\bullet}$ should be treated as tentative, and an assignment to an O_2^- species cannot be excluded, although these centers tend to have lower g_z values.

Signals similar to III (g_{iso}=2.0034) have been attributed to localization of electrons at oxygen vacancies or so-called $V_O^{\cdot}$ centres ($V_O^{\cdot\cdot}+e^- \rightarrow V_O^{\cdot}$)[65]. It should be noted that the assignment of the g=2.0034 signal is still debated in literature; this feature has, amongst others, been linked to point defects hosted in the particle-particle interfaces[66]. In any case, these signals only constitute 1% of all observed EPR signals (Table 2).

Table 2. Principal g values of the 4 different species identified by light-induced X-band and W-band EPR in the ANS sample. The Ti^{3+} center was also present in dark, but increased upon light illumination. A tentative assignment of the species I-III, as well as the percentage of their contributions are given. Further details on the assignment are given in the text.

	Tentative assignment	g_x	g_y	g_z	%
Ti^{3+}		1.99004(5)		1.95925(5)	33
I	O^-	2.026(1)	2.0142(2)	2.0030(5)	53
II	$HO_2^{\bullet}$ (or O_2^-)	2.0020(5)	2.0124(1)	2.040(5)	13
III	$V_O^{\cdot}$	2.0018(1)	2.0035(1)	2.0049(1)	1

The above CW-EPR results obtained at X-band are fully corroborated by the W-band EPR experiments (Figure 8). Figure 8c shows the CW-EPR spectrum obtained by subtracting the dark signal from the one measured after 1h illumination at 50 K with 350.7 nm laser light. Spectrum (c) was recorded at 50K to avoid saturation of the photogenerated oxygen related signals I-II and signal III, which have longer electronic relaxation times than Ti^{3+}. The corresponding simulation

(spectrum (c')) is obtained with the same species used for X-band, confirming the above discussed assignments. A detailed view of the individual EPR signals contributing to spectrum (c') is presented in Figure S8, supporting information. Notice that the higher resolution in ***g*** at W-band compared to X-band allowed us to optimize the *g* values of the observed species with higher precision (Table 2), which is best illustrated by the slight rhombicity determined for species III. The feature corresponding to the g_z value of center II (low-field signal) can only be achieved from the corresponding ESE-detected EPR spectrum (Figure 8a,a'). While these features are lost in the first derivative of the spectrum due to the large linewidth (Figure 8b,c), this is still visible in the ESE-detected absorption spectrum (Figure 8a). The line broadening may suggest that a multitude of similar species in slightly different local environments contribute to this signal, since line broadening through an excess of molecular oxygen can be excluded under the used experimental procedure (see Methods section). This broadening will mask all proton hyperfine couplings.

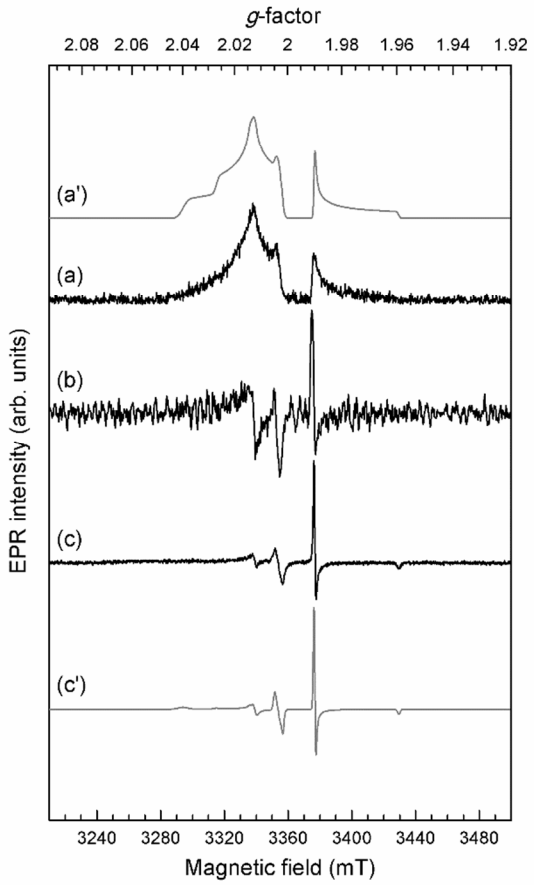

Figure 8. W-band ESE-detected EPR spectrum (a) and its first derivative (b) of ANS recorded at 10K after 2h illumination in air with 350.7nm laser light. Spectrum (c) is the difference W-band CW-EPR spectrum before and after illumination for 1h in the same conditions at 50K. Simulated spectra (a') and (c') are plotted in grey.

In summary, the X- and W-band EPR experiments indicate that before illumination the ANS sample exhibits no terminating surface Ti^{3+} centers, only bulk Ti^{3+} due to F-doping during the synthesis and no reactive surface radicals. These results were also confirmed by the ABF-STEM and STEM-EELS measurements where it was shown that the terminating surface layer consists of oxygen, not titanium atoms. The STEM-EELS results also showed that the middle of the nanosheet is more anatase (Ti^{4+}) like, while the atomic layers closer to the surface are more Ti^{3+}

rich, indicating that the Ti^{3+} bulk centers measured by EPR are located predominantly in the atomic layers closest to the surface. After illumination with UV light, photo-generated electrons interact with air to form $HO_2^{\bullet}$ (or O_2^-). The EPR signals due to bulk Ti^{3+} centers increase upon UV-irradiation, but no contribution of surface Ti^{3+} is detected. This is again in line with the high-resolution ABF-STEM images (

Figure 3), showing that oxygen atoms form the final layer of the nanoslabs. Furthermore, this also shows that the main mechanism for the observed $HO_2^{\bullet}/O_2^-$ formation during illumination is the direct transfer of conduction-band electrons to molecular oxygen ($O_2 + e^- \rightarrow O_2^-$), instead of via O_2 interaction with surface Ti^{3+} sites. The significant increase of bulk Ti^{3+} during UV illumination suggests also that electrons produced by charge separation are partially trapped at Ti^{4+} lattice ions before reaching the surface. Moreover O^- species are also observed at the surface due to hole trapping but the related O_3^- species that are often observed in UV photoexcited TiO_2 materials irradiated in air, have not been detected in the present study. This may be due to the known stabilization of surface O^- species by surface water[57].

Ab initio calculations on anatase TiO_2 were performed to study the anisotropic charge-carrier mobility and the dependence of the surface termination on the band edge positions, both properties that could influence the photocatalytic activity. In order to facilitate any photocatalytic reaction, the photoexcited electrons and holes in anatase must first reach the surface. The ease with which these charge carriers can reach the surface is influenced by their mobility. This mobility is inversely proportional to their effective mass in the anatase lattice. This effective mass is, in general, anisotropic and thus the charge carriers may reach certain surfaces easier than others. If the charge carriers more easily reach a specific surface, this is then expected to have a positive influence on the photocatalytic activity of that specific surface orientation.

We calculated the effective masses around the valence band maximum (VBM) and conduction band minimum (CBM) within the LDA+U approach. The CBM in anatase was found to be located at the Γ-point of the Brillouin zone, while the VBM is found to be on the Γ-M line, close to the M-point (½ ½ 0). The obtained values for the effective masses, relative to the bare electron mass, are listed in Table 3. Our results are consistent with published results using other choices for the exchange-correlation functional[67,68]

Table 3. Calculated effective masses for holes and electrons in anatase relative to the bare electron mass, for different lattice directions, around the valence band maximum (VBM) and the conduction band minimum (CBM).

	Lattice direction	Effective mass
m_e at CBM (Γ)	[1 0 0]	0.41
	[0 1 0]	0.41
	[0 0 1]	3.66
m_h at VBM (M-Γ)	[1 1 0]	1.69
	[1 -1 0]	2.17
	[0 0 1]	0.99

Note that the electron effective mass in the [001] direction is an order of magnitude larger than that of the electron mass in the other directions, and almost twice as large as the highest hole mass. This large electron mass anisotropy in anatase was also found experimentally[69].This very high effective mass of electrons in the [001] direction means that it is more difficult for electrons to reach the {001} surface than any other surface, which is unfavorable for photocatalytic activity in samples with a high amount of {001} surface area. The effective mass of holes in the [001] direction is actually found to be the lowest of all investigated directions. However, since the electron effective mass is much higher still, the rate at which the electrons reach the {001}

surface is the limiting factor, as we assume that the electrons play a more dominant role in the radical formation at the titania surface, having the largest influence on the photocatalytic performance.

Another important element is the position of the band edges with respect to the energy levels of the chemical reactions one wants to induce. The presence of adsorbed atoms on the surface and absorbed atoms near the surface may create a surface dipole that can shift the band edge positions and thus influences the photocatalytic activity. The experimental characterization has shown an increased fluorine concentration at the surface. To understand its influence on the band edge positions, we studied slab structures with the {001} surface with different surface terminations. We started with the clean anatase {001} surface (Figure 9(a)) and compared this to the same surface, but fully covered with H and F atoms (Figure 9(b)). Both relaxed structures are compatible with the structure deduced from the STEM and XRD measurements shown in Figure 3. But, as also shown in Ref. 63, these are not the only compatible surfaces. Also in a completely fluorinated {001} surface as shown in Figure 9(c) the Ti columns at the surface are still close to their bulk positions.

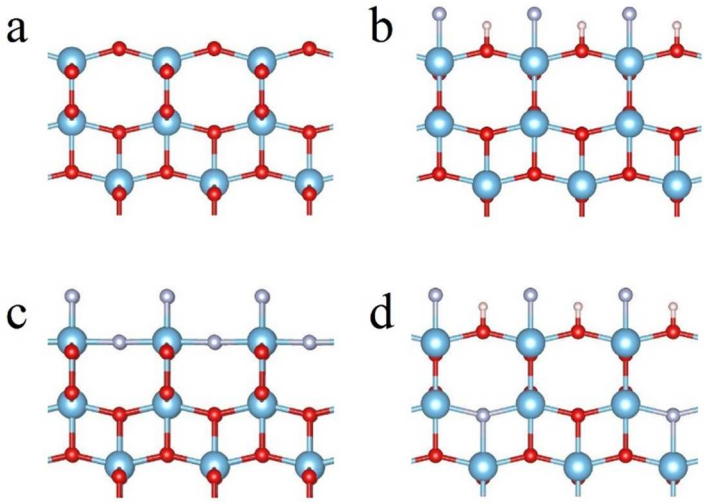

Figure 9. Anatase {001} surfaces with different terminations: (a) clean surface, (b) a fully HF-covered surface with H atoms bound to the O atoms and F atoms bound to the Ti atoms, (c) a completely fluorinated surface, and (d) a slab with a fully HF-covered surface doped with extra F atoms at O positions.

Our calculations indicate that the HF-covered surface shifts the bands down with 1.4 eV with respect to the clean case, while the fully fluorinated surface shifts the bands down with 2.2 eV. As the F atoms are also observed in the sample but close to the surface, it is also interesting to investigate the effect of F absorption on the band positions. Therefore, we replaced layers of O atoms (partly) with F atoms, for different distances to the surface. An example of such a slab in which a quarter of the fourth layer of O atoms is replaced with F atoms is shown in Figure 9(d). This creates free charge carriers in the sample, which will try to minimize the surface dipole again. This leads thus to an upwards band shift with respect to the fully HF-covered surface. The effect is largest for F atoms absorbed closest to the surface (i.e. in the second atomic layer, absorption in the first layer is unstable). In this case the bands shift upwards with 0.6 eV, but in total this still leads to a large downward shift of the bands with respect to the clean surface. These strong band shifts due to the presence of F atoms at the surface indicate why it can be expected that the prepared ANS samples with a large amount of {001} surface, but with a large concentration of fluorine atoms near the surface, show a different photocatalytic activity compared to clean surfaces.

The calculations also indicate that the extra charges due to the replacement of O by F atoms are mainly located on the Ti atoms in the second layer of Ti atoms closest to the surface, thus not at

the Ti atoms closest to the surface. This is in agreement with the EPR measurements, which indicated that the Ti^{3+} is situated on a bulk regular position and not directly at the surface.

CONCLUSIONS

Anatase catalyst materials with exposed {001} facets gain a lot of interest for photocatalytic applications. Anatase {001} nanosheets have been prepared hydrothermally using a high concentration of hydrofluoric acid. The obtained catalyst material has been tested photocatalytically towards the degradation of the cationic Rhodamine 6G dye and the anionic Methyl Orange dye, and compared with a reference anatase TiO_2 catalyst. To fully understand the structure-to–activity relation of fluorinated anatase {001} nanosheets, combined experimental and computational methods have been exploited. High-Resolution Scanning Transmission Electron Microscopy was used to fully characterize the synthesized material. Electron tomography confirms the nanosheet morphology of the TiO_2 material. The surface structure and composition of a single nanosheet was obtained by ABF-STEM and STEM-EELS. It could be detected that the final surface layer of the nanosheet consists of columns of light atoms, and that F^- is present at the surface of the nanosheets. Furthermore, Ti^{3+} was detected in the atomic layers near the surface.

However, in photocatalysis, these anatase nanosheets with exposed {001} facets reveal a significantly lower photocatalytic activity compared to the reference anatase. In order to understand the mechanism for this low catalytic performance, and to investigate the role of the presence of F^-, light-induced EPR experiments were performed. The EPR results reveal the presence of characteristic Ti^{3+} species in anatase titania before illumination and show that these are not directly at the surface as corroborated by the *ab-initio* computations. Furthermore, EPR

allows the analysis of the photo-induced paramagnetic species. Upon activation by UV light, there is a direct transfer of photo-generated conduction-band electrons to molecular oxygen, generating $HO_2^{\bullet}/O_2^-$ at the surface. The EPR-signals due to bulk Ti^{3+} centres increase, but no contribution of terminating surface Ti^{3+} is detected. This is again in good agreement with ABF-STEM showing that oxygen atoms form the final layer of the nanosheets. Moreover, O^- species are also observed at the surface due to hole trapping.

Finally, *ab-initio* calculations of the anisotropic effective mass of electrons and electron holes in anatase were performed, showing a very high effective mass of electrons in the [001] direction, having a negative impact on the mobility of electrons towards the {001} surface and thus the photocatalysis. Our *ab-initio* calculations also indicate that the presence of fluorine atoms at the surface, as evidenced by the experimental measurements, significantly lower the position of the band edges in anatase, further hindering the photocatalytic activity.

ASSOCIATED CONTENT

Supporting Information: EDS spectrum, XRD pattern of ANS sample, UV-DR measurements, degradation of Methyl Orange compared with degradation of Rhodamine 6G, additional EPR spectra. This material is available free of charge via the Internet at http://pubs.acs.org.

AUTHOR INFORMATION

Corresponding Author

*Pegie Cool, pegie.cool@uantwerpen.be

AKNOWLEDGEMENTS

Authors acknowledge the University of Antwerp for financial support in the frame of a GOA project. S.B. acknowledges funding from the European Research Council under the Seventh Framework Program (FP7), ERC Grant No. 335078 COLOURATOM. S. V. D. and V. M. acknowledge funding from the Fund for Scientific Research – Flanders (G.0687.13). T.A. acknowledges financial support from the Research Foundation Flanders (FWO, Belgium) through a post-doctoral grant.

REFERENCES

(1) Friedmann, D.; Mendive, C.; Bahnemann, D. TiO_2 for Water Treatment: Parameters Affecting the Kinetics and Mechanisms of Photocatalysis. *Appl. Catal. B Environ.* **2010**, *99*, 398–406.

(2) Kongsuebchart, W.; Praserthdam, P.; Panpranot, J.; Sirisuk, A.; Supphasrirongjaroen, P.; Satayaprasert, C. Effect of Crystallite Size on the Surface Defect of Nano- TiO_2 Prepared via Solvothermal Synthesis. *J. Cryst. Growth* **2006**, *297*, 234–238.

(3) Pan, X.; Yang, M.-Q.; Fu, X.; Zhang, N.; Xu, Y.-J. Defective TiO_2 with Oxygen Vacancies: Synthesis, Properties and Photocatalytic Applications. *Nanoscale* **2013**, *5*, 3601–3614.

(4) Zhang, L.; Mohamed, H. H.; Dillert, R.; Bahnemann, D. Kinetics and Mechanisms of Charge Transfer Processes in Photocatalytic Systems: A Review. *J. Photochem. Photobiol.*

C Photochem. Rev. **2012**, *13*, 263–276.

(5) Liu, G.; Yang, H. G.; Pan, J.; Yang, Y. Q.; Lu, G. Q. M.; Cheng, H.-M. Titanium Dioxide Crystals with Tailored Facets. *Chem. Rev.* **2014**, *114*, 9559–9612.

(6) Diebold, U. The Surface Science of Titanium Dioxide. *Surf. Sci. Rep.* **2003**, *48*, 53–229.

(7) Lazzeri, M.; Vittadini, A.; Selloni, A. Structure and Energetics of Stoichiometric TiO_2 Anatase Surfaces. *Phys. Rev. B* **2001**, *63*, 155409.

(8) Selloni, A. Anatase Shows Its Reactive Side. *Nat. Mater.* **2008**, *7*, 613–615.

(9) Vittadini, A.; Selloni, A.; Rotzinger, F. P.; Grätzel, M. Structure and Energetics of Water Adsorbed at TiO_2 Anatase (101) and (001) Surfaces. *Phys. Rev. Lett.* **1998**, *81*, 2954–2957.

(10) Diebold, U.; Ruzycki, N.; Herman, G. S.; Selloni, a. One Step towards Bridging the Materials Gap: Surface Studies of TiO_2 Anatase. *Catal. Today* **2003**, *85*, 93–100.

(11) Barnard, A. S.; Curtiss, L. A. Prediction of TiO_2 Nanoparticle Phase and Shape Transitions Controlled by Surface Chemistry. *Nano Lett.* **2005**, *5*, 1261–1266.

(12) Yang, H. G.; Sun, C. H.; Qiao, S. Z.; Zou, J.; Liu, G.; Smith, S. C.; Cheng, H. M.; Lu, G. Q. Anatase TiO_2 Single Crystals with a Large Percentage of Reactive Facets. *Nature* **2008**, *453*, 638–641.

(13) Han, X.; Kuang, Q.; Jin, M.; Xie, Z.; Zheng, L. Synthesis of Titania Nanosheets with a High Percentage of Exposed (001) Facets and Related Photocatalytic Properties. *J. Am. Chem. Soc.* **2009**, *131*, 3152–3153.

(14) Xiang, Q.; Lv, K.; Yu, J. Pivotal Role of Fluorine in Enhanced Photocatalytic Activity of Anatase TiO_2 Nanosheets with Dominant (001) Facets for the Photocatalytic Degradation of Acetone in Air. *Appl. Catal. B Environ.* **2010**, *96*, 557–564.

(15) Yang, X. H.; Li, Z.; Liu, G.; Xing, J.; Sun, C.; Yang, H. G.; Li, C. Ultra-Thin Anatase TiO_2 Nanosheets Dominated with {001} Facets: Thickness-Controlled Synthesis, Growth Mechanism and Water-Splitting Properties. *CrystEngComm* **2011**, *13*, 1378.

(16) Wu, Q.; Liu, M.; Wu, Z.; Li, Y.; Piao, L. Is Photooxidation Activity of {001} Facets Truly Lower Than That of {101} Facets for Anatase TiO_2 Crystals? *J. Phys. Chem. C* **2012**, *116*, 26800–26804.

(17) Zhang, J.; Chen, W.; Xi, J.; Ji, Z. {001} Facets of Anatase TiO_2 Show High Photocatalytic Selectivity. *Mater. Lett.* **2012**, *79*, 259–262.

(18) Dozzi, M.; Selli, E. Specific Facets-Dominated Anatase TiO_2: Fluorine-Mediated Synthesis and Photoactivity. *Catalysts* **2013**, *3*, 455–485.

(19) Pan, J.; Liu, G.; Lu, G. Q. M.; Cheng, H.-M. On the True Photoreactivity Order of {001}, {010}, and {101} Facets of Anatase TiO_2 Crystals. *Angew. Chem. Int. Ed. Engl.* **2011**, *50*, 2133–2137.

(20) Gordon, T. R.; Cargnello, M.; Paik, T.; Mangolini, F.; Weber, R. T.; Fornasiero, P.; Murray, C. B. Nonaqueous Synthesis of TiO_2 Nanocrystals Using TiF_4 to Engineer Morphology, Oxygen Vacancy Concentration, and Photocatalytic Activity. *J. Am. Chem. Soc.* **2012**, *134*, 6751–6761.

(21) Tachikawa, T.; Yamashita, S.; Majima, T. Evidence for Crystal-Face-Dependent TiO_2

Photocatalysis from Single-Molecule Imaging and Kinetic Analysis. *J. Am. Chem. Soc.* **2011**, *133*, 7197–7204.

(22) Liu, S.; Yu, J.; Cheng, B.; Jaroniec, M. Fluorinated Semiconductor Photocatalysts: Tunable Synthesis and Unique Properties. *Adv. Colloid Interface Sci.* **2012**, *173*, 35–53.

(23) Czoska, A. M.; Livraghi, S.; Chiesa, M.; Giamello, E.; Agnoli, S.; Granozzi, G.; Finazzi, E.; Valentin, C. Di; Pacchioni, G.; Di Valentin, C.; et al. The Nature of Defects in Fluorine-Doped TiO_2. *J. Phys. Chem. C* **2008**, *112*, 8951–8956.

(24) Yu, J. C.; Yu; Ho; Jiang; Zhang; Jimmy C. Yu Jiaguo Yu, Wingkei Ho, Zitao Jiang, L. Z. C. Effects of F-Doping on the Photocatalytic Activity and Microstructures of Nanocrystalline TiO_2 Powders. *Chem. Mater.* **2002**, *14*, 3808–3816.

(25) Sofianou, M.-V.; Psycharis, V.; Boukos, N.; Vaimakis, T.; Yu, J.; Dillert, R.; Bahnemann, D.; Trapalis, C. Tuning the Photocatalytic Selectivity of TiO_2 Anatase Nanoplates by Altering the Exposed Crystal Facets Content. *Appl. Catal. B Environ.* **2013**, *142–143*, 761–768.

(26) Barbieriková, Z.; Dvoranová, D.; Sofianou, M.-V.; Trapalis, C.; Brezová, V. UV-Induced Reactions of Mg^{2+}-Doped Anatase Nanocrystals with Exposed {001} Facets: An EPR Study. *J. Catal.* **2015**, *331*, 39–48.

(27) Midgley, P. A; Weyland, M. 3D Electron Microscopy in the Physical Sciences: The Development of Z-Contrast and EFTEM Tomography. *Ultramicroscopy* **2003**, *96*, 413–431.

(28) Bals, S.; Batenburg, K. J.; Verbeeck, J.; Sijbers, J.; Van Tendeloo, G. Quantitative Three-

Dimensional Reconstruction of Catalyst Particles for Bamboo-like Carbon Nanotubes. *Nano Lett.* **2007**, *7*, 3669–3674.

(29) Schlossmacher, P.; Klenov, D. O.; Freitag, B.; von Harrach, H. S. Enhanced Detection Sensitivity with a New Windowless XEDS System for AEM Based on Silicon Drift Detector Technology. *Micros. Today* **2010**, *18*, 14–20.

(30) Batenburg, K. J.; Bals, S.; Sijbers, J.; Kübel, C.; Midgley, P. A.; Hernandez, J. C.; Kaiser, U.; Encina, E. R.; Coronado, E. A.; Tendeloo, G. Van. 3D Imaging of Nanomaterials by Discrete Tomography. *Ultramicroscopy* **2009**, *109*, 730–740.

(31) Stoll, S.; Schweiger, A. EasySpin, a Comprehensive Software Package for Spectral Simulation and Analysis in EPR. *J. Magn. Reson.* **2006**, *178*, 42–55.

(32) Kus, M.; Ribbens, S.; Meynen, V.; Cool, P. Microvolume TOC Analysis as Useful Tool in the Evaluation of Lab Scale Photocatalytic Processes. *Catalysts* **2013**, *3*, 74–87.

(33) Hohenberg, P.; Kohn, W. Inhomogeneous Electron Gas. *Phys. Rev.* **1964**, *136*, B864–B871.

(34) Kohn, W.; Sham, L. Self-Consistent Equations Including Exchange and Correlation Effects. *Phys. Rev.* **1965**, *140*, A1133–A1138.

(35) Blöchl, P. E. Projector Augmented-Wave Method. *Phys. Rev. B* **1994**, *50*, 17953–17979.

(36) Anisimov, V. I.; Zaanen, J.; Andersen, O. K. Band Theory and Mott Insulators: Hubbard U instead of Stoner I. *Phys. Rev. B* **1991**, *44*, 943–954.

(37) Anisimov, V. I.; Solovyev, I. V.; Korotin, M. A.; Czyżyk, M. T.; Sawatzky, G. A. Density-

Functional Theory and NiO Photoemission Spectra. *Phys. Rev. B* **1993**, *48*, 16929–16934.

(38) Arroyo-de Dompablo, M. E.; Morales-García, A.; Taravillo, M. DFT+ U Calculations of Crystal Lattice, Electronic Structure, and Phase Stability under Pressure of TiO_2 Polymorphs. *J. Chem. Phys.* **2011**, *135*, 54503.

(39) Fonari, A.; Sutton, C. Effective Mass Calculator. **2012**.

(40) Batenburg, K. J.; Sijbers, J. Dart: A Fast Heuristic Algebraic Reconstruction Algorithm for Discrete Tomography. In *2007 IEEE International Conference on Image Processing*; IEEE, 2007; Vol. TP-L5.2., p IV-133-IV-136.

(41) Batenburg, K. J.; Sijbers, J. DART: A Practical Reconstruction Algorithm for Discrete Tomography. *IEEE Trans. Image Process.* **2011**, *20*, 2542–2553.

(42) Ishikawa, R.; Okunishi, E.; Sawada, H.; Kondo, Y.; Hosokawa, F.; Abe, E. Direct Imaging of Hydrogen-Atom Columns in a Crystal by Annular Bright-Field Electron Microscopy. *Nat. Mater.* **2011**, *10*, 278–281.

(43) Howard, C. J.; Sabine, T. M.; Dickson, F. Structural and Thermal Parameters for Rutile and Anatase. *Acta Crystallogr. Sect. B* **1991**, *47*, 462–468.

(44) Ebraheem, S.; El-Saied, A. Band Gap Determination from Diffuse Reflectance Measurements of Irradiated Lead Borate Glass System Doped with TiO_2 by Using Diffuse Reflectance Technique. *Mater. Sci. Appl.* **2013**, *4*, 324–329.

(45) Liu, S.; Yu, J.; Jaroniec, M. Tunable Photocatalytic Selectivity of Hollow TiO_2 Microspheres Composed of Anatase Polyhedra with Exposed {001} Facets. *J. Am. Chem.*

Soc. **2010**, *132*, 11914–11916.

(46) Zhu, J.; Wang, S.; Bian, Z.; Xie, S.; Cai, C.; Wang, J.; Yang, H.; Li, H. Solvothermally Controllable Synthesis of Anatase TiO_2 Nanocrystals with Dominant {001} Facets and Enhanced Photocatalytic Activity. *CrystEngComm* **2010**, *12*, 2219.

(47) Amano, F.; Yasumoto, T.; Mahaney, O. O. P.; Uchida, S.; Shibayama, T.; Terada, Y.; Ohtani, B. Highly Active Titania Photocatalyst Particles of Controlled Crystal Phase, Size, and Polyhedral Shapes. *Top. Catal.* **2010**, *53*, 455–461.

(48) Hurum, D. C.; Agrios, A. G.; Gray, K. A.; Rajh, T.; Thurnauer, M. C. Explaining the Enhanced Photocatalytic Activity of Degussa P25 Mixed-Phase TiO_2 Using EPR. *J. Phys. Chem. B* **2003**, *107*, 4545–4549.

(49) Hurum, D. C.; Agrios, A. G.; Crist, S. E.; Gray, K. A.; Rajh, T.; Thurnauer, M. C. Probing Reaction Mechanisms in Mixed Phase TiO_2 by EPR. *J. Electron Spectros. Relat. Phenomena* **2006**, *150*, 155–163.

(50) Livraghi, S.; Chiesa, M.; Paganini, M. C.; Giamello, E. On the Nature of Reduced States in Titanium Dioxide As Monitored by Electron Paramagnetic Resonance. I: The Anatase Case. *J. Phys. Chem. C* **2011**, *115*, 25413–25421.

(51) Chiesa, M.; Paganini, M. C.; Livraghi, S.; Giamello, E. Charge Trapping in TiO_2 Polymorphs as Seen by Electron Paramagnetic Resonance Spectroscopy. *Phys. Chem. Chem. Phys.* **2013**, *15*, 9435–9447.

(52) Howe, R. F.; Gratzel, M. EPR Study of Hydrated Anatase under UV Irradiation. *J. Phys. Chem.* **1987**, *91*, 3906.

(53) Fittipaldi, M.; Gatteschi, D.; Fornasiero, P. The Power of EPR Techniques in Revealing Active Sites in Heterogeneous Photocatalysis: The Case of Anion Doped TiO_2. *Catal. Today* **2013**, *206*, 2–11.

(54) Anpo, M.; Che, M.; Fubini, B.; Garrone, E. Generation of Superoxide Ions at Oxide Surfaces. *Top. Catal.* **1999**, *8*, 189–198.

(55) Micic, O. I.; Zhang, Y. N.; Cromack, K. R.; Trifunac, A. D.; Thurnauer, M. C. Trapped Holes on TiO_2 Colloids Studied By Electron-Paramagnetic-Resonance. *J. Phys. Chem.* **1993**, *97*, 7277–7283.

(56) Kumar, C. P.; Gopal, N. O.; Wang, T. C.; Wong, M.-S.; Ke, S. C. EPR Investigation of TiO_2 Nanoparticles with Temperature-Dependent Properties. *J. Phys. Chem. B* **2006**, *110*, 5223–5229.

(57) Panarelli, E. G.; Livraghi, S.; Maurelli, S.; Polliotto, V.; Chiesa, M.; Giamello, E. Role of Surface Water Molecules in Stabilizing Trapped Hole Centres in Titanium Dioxide (Anatase) as Monitored by Electron Paramagnetic Resonance. *J. Photochem. Photobiol. A Chem.* **2016**, *322–323*, 27–34.

(58) Thompson, T. L.; Yates, J. T. Surface Science Studies of the Photoactivation of TiO_2 - New Photochemical Processes. *Chem. Rev.* **2006**, *106*, 4428–4453.

(59) Attwood, A. L.; Murphy, D. M.; Edwards, J. L.; Egerton, T. A.; Harrison, R. W. An EPR Study of Thermally and Photochemically Generated Oxygen Radicals on Hydrated and Dehydrated Titania Surfaces. *Res. Chem. Intermed.* **2003**, *29*, 449–465.

(60) Brezová, V.; Barbieriková, Z.; Zukalová, M.; Dvoranová, D.; Kavan, L. EPR Study of ^{17}O-

Enriched Titania Nanopowders under UV Irradiation. *Catal. Today* **2014**, *230*, 112–118.

(61) Green, J.; Carter, E.; Murphy, D. M. An EPR Investigation of Acetonitrile Reactivity with Superoxide Radicals on Polycrystalline TiO_2. *Res. Chem. Intermed.* **2009**, *35*, 145–154.

(62) Srinivas, D.; Manikandan, P.; Laha, S. C.; Kumar, R.; Ratnasamy, P. Reactive Oxo-Titanium Species in Titanosilicate Molecular Sieves: EPR Investigations and Structure–activity Correlations. *J. Catal.* **2003**, *217*, 160–171.

(63) Wang, Y.; Zhang, H.; Han, Y.; Liu, P.; Yao, X.; Zhao, H. A Selective Etching Phenomenon on {001} Faceted Anatase Titanium Dioxide Single Crystal Surfaces by Hydrofluoric Acid. *Chem. Commun. (Camb).* **2011**, *47*, 2829–2831.

(64) Catton, R. C.; Symons, M. C. R. Unstable Intermediates. Part LX. HO_2 Radical in γ-Irradiated Strontium Chloride Hexahydrate. *J. Chem. Soc. A* **1969**, 1393–1395.

(65) Riss, A.; Berger, T.; Stankic, S.; Bernardi, J.; Knözinger, E.; Diwald, O. Charge Separation in Layered Titanate Nanostructures: Effect of Ion Exchange Induced Morphology Transformation. *Angew. Chemie - Int. Ed.* **2008**, *47*, 1496–1499.

(66) Baumann, S. O.; Elser, M. J.; Auer, M.; Bernardi, J.; Hüsing, N.; Diwald, O. Solid−Solid Interface Formation in TiO_2 Nanoparticle Networks. *Langmuir* **2011**, *27*, 1946–1953.

(67) Huy, H. A.; Aradi, B.; Frauenheim, T.; Deák, P. Calculation of Carrier-Concentration-Dependent Effective Mass in Nb-Doped Anatase Crystals of TiO_2. *Phys. Rev. B* **2011**, *83*, 155201.

(68) Lany, S. Semiconducting Transition Metal Oxides. *J. Phys. Condens. Matter* **2015**, *27*,

283203.

(69) Hirose, Y.; Yamada, N.; Nakao, S.; Hitosugi, T.; Shimada, T.; Hasegawa, T. Large Electron Mass Anisotropy in a d-Electron-Based Transparent Conducting Oxide: Nb-Doped Anatase TiO_2 Epitaxial Films. *Phys. Rev. B* **2009**, *79*, 165108.

TOC graphic

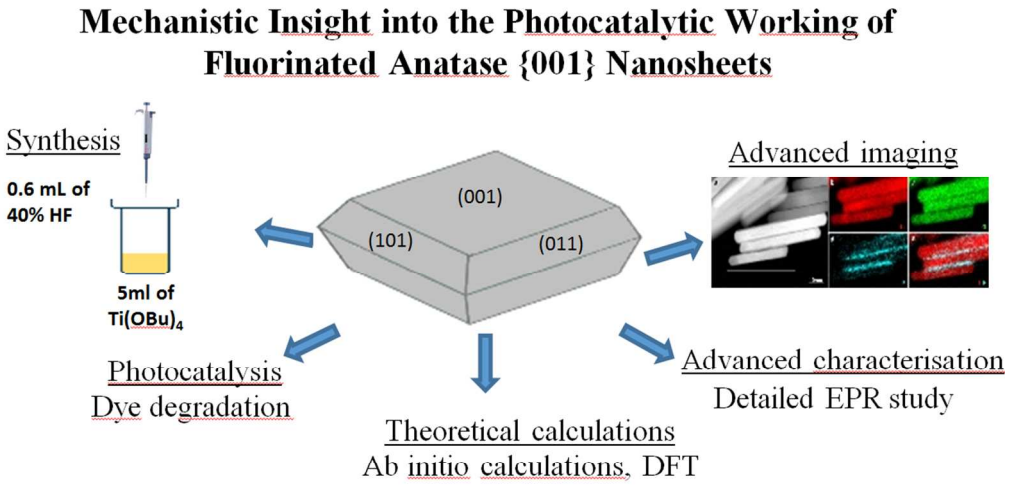
Mechanistic Insight into the Photocatalytic Working of Fluorinated Anatase {001} Nanosheets
Synthesis
0.6 mL of 40% HF
5ml of Ti(OBu)4
(001)
(101)
(011)
Advanced imaging
Photocatalysis
Dye degradation
Theoretical calculations
Ab initio calculations, DFT
Advanced characterisation
Detailed EPR study

Mechanistic Insight into the Photocatalytic Working of Fluorinated Anatase{001} Nanosheets

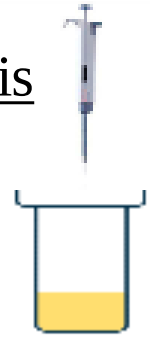

Synthesis

0.6 mL of 40% HF

5ml of $Ti(OBu)_4$

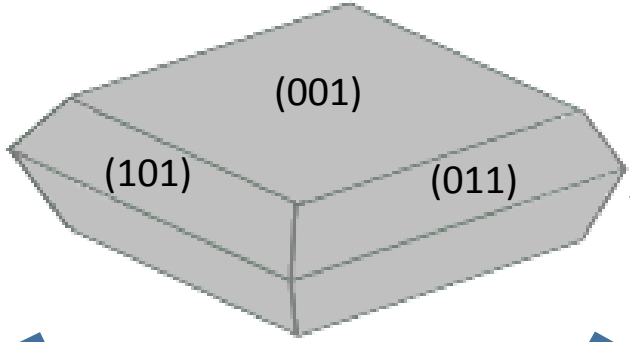

Advanced imaging

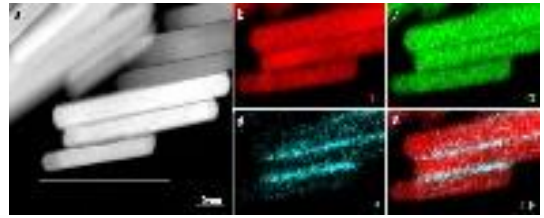

Photocatalysis

Dye degradation

Theoretical calculations

Ab initio calculations, DFT

Advanced characterisation

Detailed EPR study